



Trans. Nonferrous Met. Soc. China 35(2025) 446-459

Transactions of Nonferrous Metals Society of China

www.tnmsc.cn



Effect of secondary phases on corrosion behavior of Mg-7Sn-1Zn-1Y alloys

Xue-jian WANG¹, Hua-qiang XIAO¹, Chong WANG², En-yu GUO^{2,3}, Tong-min WANG^{2,3}, Bo LIN¹

- 1. School of Mechanical Engineering, Guizhou University, Guiyang 550000, China;
- 2. Key Laboratory of Solidification Control and Digital Preparation Technology (Liaoning Province), School of Materials Science and Engineering, Dalian University of Technology, Dalian 116024, China;
 - 3. Ningbo Institute of Dalian University of Technology, Ningbo 315000, China

Received 6 June 2023; accepted 27 February 2024

Abstract: Microstructural characterization, mass loss tests, hydrogen evolution tests, electrochemical measurements, and corrosion morphology observations were conducted to investigate the effect of the secondary phases on the corrosion behavior of the as-cast Mg-7Sn-1Zn-1Y (TZW711) alloy after solution treatment (T4) and aging treatment (T6). The results show that the T4-TZW711 alloy possesses the highest corrosion resistance in the early corrosion stage. This is because the dissolution of Mg₂Sn reduces the cathodic current density and increases the charge transfer resistance (*R*_{ct}). When the corrosion time is prolonged, the undissolved and clustered MgSnY phase will peel off from the T4-TZW711 alloy surface, thereby increasing the corrosion rate of the alloy. After aging treatment, the undissolved MgSnY phase is dispersed, which results in a lower localized corrosion sensitivity of T6-TZW711 alloy than that of the T4-TZW711 alloy, suggesting that the T6 treatment can enhance the corrosion resistance of Mg-7Sn-1Zn-1Y alloys. **Key words:** Mg-Sn-Zn-Y alloy; heat treatment; MgSnY phase; electrochemical test; corrosion behavior

1 Introduction

Mg–Sn-based alloys have recently drawn substantial attention on account of their potential use for the development of new types of Mg alloys with high creep resistance and age hardening characteristics [1–3]. The superior creep resistance of Mg–Sn alloys can be ascribed to the presence of Mg₂Sn precipitates with a melting point of 770.5 °C, which is higher than that of α -Mg [4,5]. Moreover, the maximum solid solubility of the Sn element in α -Mg at the eutectic temperature of 561 °C is 14.85 wt.%, which decreases sharply to 0.45 wt.% at 200 °C [6], indicating the capability of improving the mechanical properties via the precipitation hardening of Mg₂Sn. The tensile yield strength of

Mg–Sn alloys exceeds 350 MPa at room temperature [7]. However, recent studies have reported that the corrosion resistance of the Mg–Sn alloys deteriorates with increasing Mg₂Sn phase content [8–10]. This is due to the higher corrosion potential of Mg₂Sn in comparison with that of α -Mg. Thus, Mg₂Sn can act as a cathodic phase that accelerates the corrosion of Mg–Sn alloys. In order to realize the industrialization of Mg–Sn alloys, it is highly worthwhile to investigate the corrosion mechanism and enhance the corrosion resistance of Mg–Sn alloys.

Secondary phases have a vital effect on the corrosion behavior of Mg-Sn alloys. Alloying, heat treatment, and deformation processing are commonly utilized to alter the size, type, content, and distribution of the secondary phase, thereby altering

the corrosion behavior of Mg-Sn alloys [11–13]. For example, LIU et al [14] investigated the effect of quantity of the Mg₂Sn phase on the corrosion behavior of Mg-7Sn alloy via solution treatment at different temperatures. The results exhibited that the corrosion resistance increased with decreasing Mg₂Sn quantity. In our previous study, the Mg₂Sn phase was refined after extrusion processing, which reduced the localized corrosion and corrosion rate of the alloy [15]. In addition, certain studies have attempted to mitigate the adverse effects of the Mg₂Sn phase on corrosion resistance of Mg-Sn alloys by adding the alloying elements [16,17]. According to HUANG et al [18], the Zn element can improve the corrosion resistance of Mg-4Sn-4Zn-2Al alloys after artificial aging treatment, which is attributed to the refined MgZn₂ precipitates. HA et al [19] reported that no Zn-related compounds were observed in the as-extruded Mg-5Sn-xZn alloys, while the passive film stability of the alloys was increased by the addition of Zn. Furthermore, the Y element is another alloying element commonly used to enhance the corrosion resistance of Mg alloys. It has been reported that the effect of Y-enriched secondary phases on the micro-galvanic corrosion of Mg alloys is rather mild [20]. In another study, LIU et al [21] reported that secondary phases containing Y element are more active than the α -Mg matrix, act as anodes, and dissolve preferentially. The corrosion products containing Y element can enhance the compactness of the corrosion film on the surface of Mg alloys [22]. Based on the above results, it can be inferred that Zn and Y can be used as alloying elements to improve the corrosion resistance of Mg-Sn alloys. Nevertheless, the corrosion behavior of Mg-Sn-Zn-Y alloys has not been satisfactorily investigated, and the relationship between the microstructure and corrosion behavior of such alloys has rarely been studied. Hence, it is essential to clarify the actual effects of secondary phases on the corrosion behavior of Mg-Sn-Zn-Y alloys, which will promote the industrial application of Mg-Sn-Zn-Y alloys.

In this work, the Mg-7Sn-1Zn-1Y alloy was selected as the research object. After being cast, the alloy was subjected to solution and aging treatments. The microstructural characterization, mass loss tests, hydrogen evolution tests, electrochemical measurements, and corrosion morphology

observations were conducted to reveal the effect of secondary phases on the corrosion behavior of the Mg-7Sn-1Zn-1Y alloy.

2 Experimental

2.1 Material preparation and microstructure characterization

Mg-7Sn-1Zn-1Y alloy ingots were prepared by melting high-purity Mg (99.99%), Sn (99.99%), Zn (99.95%), and Mg-20Y master alloy in a resistance furnace under the protection of a mixed gas atmosphere of SF₆ and CO₂. The raw materials were melted at 720 °C and the liquid metal was held in a magnesia crucible for 30 min. After a sufficient mixture of the melt, the alloy was cast into a preheated steel mold to produce a cylindrical ingot with a diameter of 80 mm and a length of 120 mm. The chemical composition (wt.%) of the cast ingot measured by inductively coupled plasma-atomic emission spectroscopy (ICP-AES, PlasmaQuant 9100, Germany) was 7.05 Sn, 1.09 Zn, 0.93 Y, 0.0078 Fe, and balance Mg. Subsequently, the as-cast ingot was subjected to a two-step solution treatment, i.e., first kept at 450 °C for 20 h and then at 480 °C for 4 h, which was followed by water quenching. Then, aging treatment was performed in a vacuum oven at 200 °C for 18 h. Hereinafter, the as-cast, solution-treated, and agingtreated specimens were denoted as as-cast TZW711, T4-TZW711, and T6-TZW711, respectively.

The phase compositions of the alloys were analyzed by X-ray diffraction (XRD; PANalytical Empyrean) with Cu K_{α} radiation and a scan range (2 θ) from 20° to 100°. The microstructure was characterized by optical microscopy (OM; Olympus GX51), electron probe micro-analyzer (EPMA; JXA–8530F Plus) equipped with a wavelength dispersive spectrometer (WDS), and transmission electron microcopy (TEM; JEOL JEM–2100F). The TEM samples were prepared by a Gatan precision ion polishing system (Gatan model 695) at a voltage of 5 kV.

2.2 Immersion and electrochemical tests

The dimensions of the samples used for the mass loss and hydrogen evolution measurements were $20 \text{ mm} \times 20 \text{ mm} \times 2 \text{ mm}$. All samples were mechanically ground to 2000 grit with SiC paper, and then immersed in 300 mL 3.5 wt.% NaCl

solution at room temperature for 72 h. The hydrogen evolution measurements were conducted following the method proposed in Ref. [23]. The samples were placed in a solution containing 200 g/L CrO₃ and 10 g/L AgNO₃ for 10 min to remove the corrosion products. The mass loss was determined by weighing the samples before and after immersion. The corrosion rate of mass loss was calculated as follows [24]:

$$C_{\rm R} = \frac{K \cdot W}{A \cdot t \cdot \rho} \tag{1}$$

where C_R is the corrosion rate (mm/a), K is a constant (8.76×10⁴), W is the mass loss (g), A is the corrosion area (cm²), t is the immersion time (h), and ρ is the density (g/cm³). In addition, the corrosion morphology and corrosion depth were observed by field emission scanning electron microscopy (FESEM; Zeiss Supra–55, Zeiss Corp.) and 3D laser confocal microscopy. The X-ray photoelectron spectroscopy (XPS; ESCALAB XI+) was used to analyze the chemical composition of the corrosion products.

Moreover, the electrochemical behavior of samples with an exposed area of 1 cm² was potentiodynamic polarization investigated via and electrochemical impedance spectroscopy (EIS) in 3.5 wt.% NaCl solution at (25±1) °C. In the measurements, a three-electrode cell containing Ag/AgCl was used as the reference electrode, a Pt foil as the counter electrode, and the sample as the working electrode. The potentiodynamic polarization curves and EIS data were measured after an initial delay of 20 min, facilitating the development of a relatively stable open circuit potential (OCP). The sweep range of the potentiodynamic polarization curves was from -300 to 150 mV (vs OCP), and the sweep rate was 1 mV/s. EIS measurement was performed in a frequency range of 10⁵-10⁻² Hz with an amplitude signal of 10 mV. It is worth noting that, for the immersion and electrochemical measurements, at least three samples were tested under each condition to ensure accuracy.

3 Results

3.1 Microstructure

Figure 1 depicts the XRD patterns of the Mg-7Sn-1Zn-1Y alloys obtained under different heat treatments. It is observed that α -Mg, Mg₂Sn, and MgSnY phases were present in the as-cast

TZW711 alloy. In the T4-TZW711 alloy, the diffraction peaks of the Mg_2Sn phase disappeared, and only α -Mg and MgSnY phases were detected. This indicated that, after solution treatment, most Mg_2Sn phases were dissolved into the α -Mg matrix. Nevertheless, the diffraction peaks of the Mg_2Sn phases reappeared in the T6-TZW711 alloy due to age precipitation. It is worth noting that no Zn-enriched phases were detected in the XRD measurements, probably due to their very low phase content.

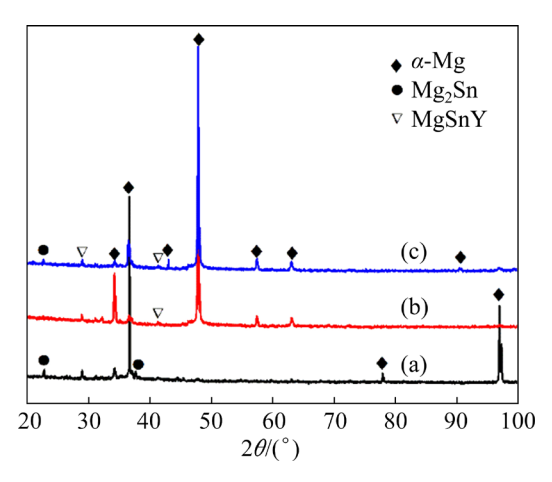


Fig. 1 XRD patterns of Mg-7Sn-1Zn-1Y alloys: (a) Ascast TZW711; (b) T4-TZW711; (c) T6-TZW711

Figure 2 presents the backscattered electron (BSE) microscopy images and corresponding EPMA elemental mappings of the Mg-7Sn-1Zn-1Y alloys. The as-cast TZW711 alloy exhibited a typical dendritic structure, consisting of dark α -Mg dendritic grains and bright secondary phases distributed along the dendrite arms. Moreover, continuous gray-network microstructures were also observed along the dendrite boundaries. In the previous study [23], these regions have been reported to be Sn-enriched areas due to the Sn element segregation ahead of the solid-liquid interface during solidification. After solution treatment, the Sn-enriched areas are eliminated. The EPMA elemental mappings revealed that the as-cast TZW711 alloy contained two types of secondary phases, i.e., non-Y-enriched phase (Point A) and Y-enriched phase (Point B). In addition, the average chemical composition of these phases was quantitatively measured by WDS, and the results are listed in Table 1. It was found that Point A was Mg₂Sn phase with a measured atomic composition of Mg_{70.2}Sn_{29.0}Zn_{0.8}. The molar ratio of Mg to Sn

deviated slightly from Mg₂Sn because a portion of the Mg came from the α -Mg matrix [25]. A small amount of Zn element was often found to be enriched around Mg₂Sn phases [26]. Points B and C were both found to be MgSnY phases with measured atomic compositions of Mg_{36.87}Sn_{32.47}Y_{30.56} and Mg_{40.65}Sn_{28.26}Y_{30.92}, respectively, indicating that the MgSnY phases were not dissolved into the α -Mg matrix after solution treatment. The WDS results regarding Points D-F also confirmed that the solution and aging treatments mainly altered the Sn content and had little effect on the Y content of the α -Mg matrix. However, the distribution of the MgSnY phase in the T4-TZW711 and T6-TZW711 alloys underwent significant changes. More specifically, the MgSnY phases first clustered and grew in the T4-TZW711 alloy, and then became distributed relatively uniformly in the T6-TZW711 alloy. The Mg₂Sn phase and interdendritic element

enrichment disappeared, and the remaining MgSnY phases were mostly distributed along grain boundaries after solution treatment. This led to the fact that the distribution of MgSnY phase was inhomogeneous in the T4-TZW711 alloy. The secondary phase area fraction of Mg-7Sn-1Zn-1Y alloy under three different conditions was calculated. The area fraction of secondary phases for as-cast TZW711, T4-TZW711, and T6-TZW711 alloys was 1.31%, 0.70%, and 0.83%, respectively. It was inferred that the Mg2Sn and MgSnY were precipitated in the T6-TZW711 alloy after aging treatment. Thus, the secondary phases showed dispersive distribution in the T6-TZW711 alloy due to the increase of area fraction of the secondary phases.

Nevertheless, as it can be observed in Fig. 2(c), no Mg₂Sn phases were found in the T6-TZW711 alloy, which did not agree with the XRD results. To

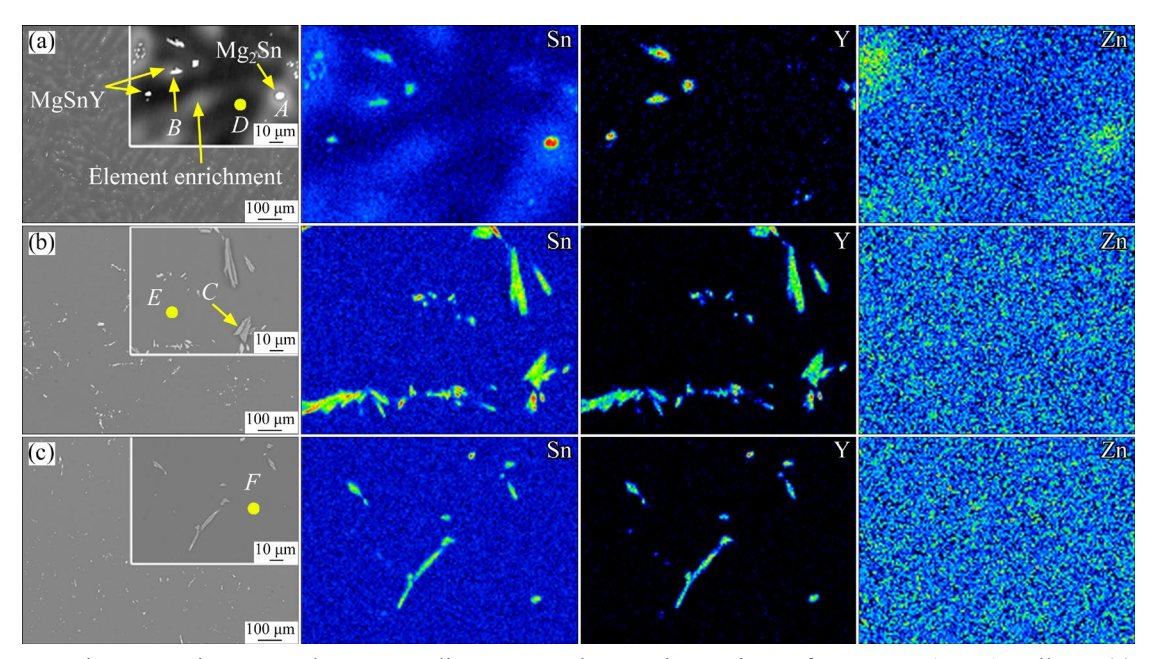


Fig. 2 BSE microscopy images and corresponding EPMA elemental mappings of Mg-7Sn-1Zn-1Y alloys: (a) As-cast TZW711; (b) T4-TZW711; (c) T6-TZW711

Table 1 Chemical compositions of points marked in Fig. 2

Point	Mg		Sn		Zn		Y	
	wt.%	at.%	wt.%	at.%	wt.%	at.%	wt.%	at.%
A	32.8	70.2	66.2	29.0	1.0	0.8	0	0
B	11.99	36.87	51.57	32.47	0.09	0.10	36.35	30.56
C	13.91	40.65	47.23	28.26	0.16	0.17	38.70	30.92
D	95.35	98.75	3.60	0.85	1.04	0.40	0.01	0.044
E	92.95	98.28	5.83	1.27	1.09	0.44	0.13	0.01
F	93.07	98.27	5.81	1.25	1.08	0.47	0.04	0.01

this end, TEM test was performed to further authenticate the microstructure of the T6-TZW711 alloy. The results are shown in Fig. 3. According to the scanning transmission electron microscopy (STEM) results and corresponding EDS elemental mappings, the bright precipitate was simultaneously enriched with Y and Sn elements, suggesting that it was MgSnY. Furthermore, the selected area electron diffraction (SAED) pattern confirmed that the two precipitates around MgSnY were Mg2Sn and MgZn₂. Thus, after aging treatment, the T6-TZW711 alloy contained MgSnY, Mg₂Sn, and MgZn₂ precipitates. It is worth noting that the MgZn₂ precipitate content was much lower than that of Mg₂Sn. It is speculated that the effect of the MgZn₂ precipitate on corrosion behavior is far weaker than that of the Mg₂Sn.

3.2 Immersion corrosion rate and electrochemical behavior

Figure 4(a) displays the corrosion rates of the Mg-7Sn-1Zn-1Y alloys determined via mass loss measurements after immersion in 3.5 wt.% NaCl solution for 24, 48, and 72 h. The corrosion rates of all alloys decreased gradually with increasing immersion time. After immersion for 24 h, the corrosion rate of the T4-TZW711 alloy was lower

than that of the as-cast TZW711 and T6-TZW711 alloys, while the difference in the corrosion rate between the T4-TZW711 and T6-TZW711 alloys became smaller with increasing immersion time. The corrosion rates of the as-cast TZW711, T4-TZW711, and T6-TZW711 alloys were (3.25 ± 0.05) , (2.42 ± 0.06) , and (2.39 ± 0.02) mm/a, respectively. Furthermore, when 1 mol Mg is corroded, this is accompanied by the production of 1 mol H₂. Hydrogen evolution rate is proportional to the corrosion rate of Mg alloys. Figure 4(b) shows the hydrogen volume variation for different Mg-7Sn-1Zn-1Y alloys as a function of the immersion time. It can be observed that, at the initial immersion stage, the difference in the hydrogen evolution rate was minor for all alloys, but it became apparent after immersion for 4 h. This indicates that the corrosion film on the alloy surface provides only transient protection [24]. The T4-TZW711 alloy exhibited the lowest hydrogen evolution rate after immersion for 36 h, which agreed well with the mass loss measurement results. However, the rapid increase in the hydrogen evolution rate of the T4-TZW711 alloy after immersion for 36 h resulted in a higher hydrogen evolution rate than that for the T6-TZW711 alloy. This may be attributed to a significant change in the

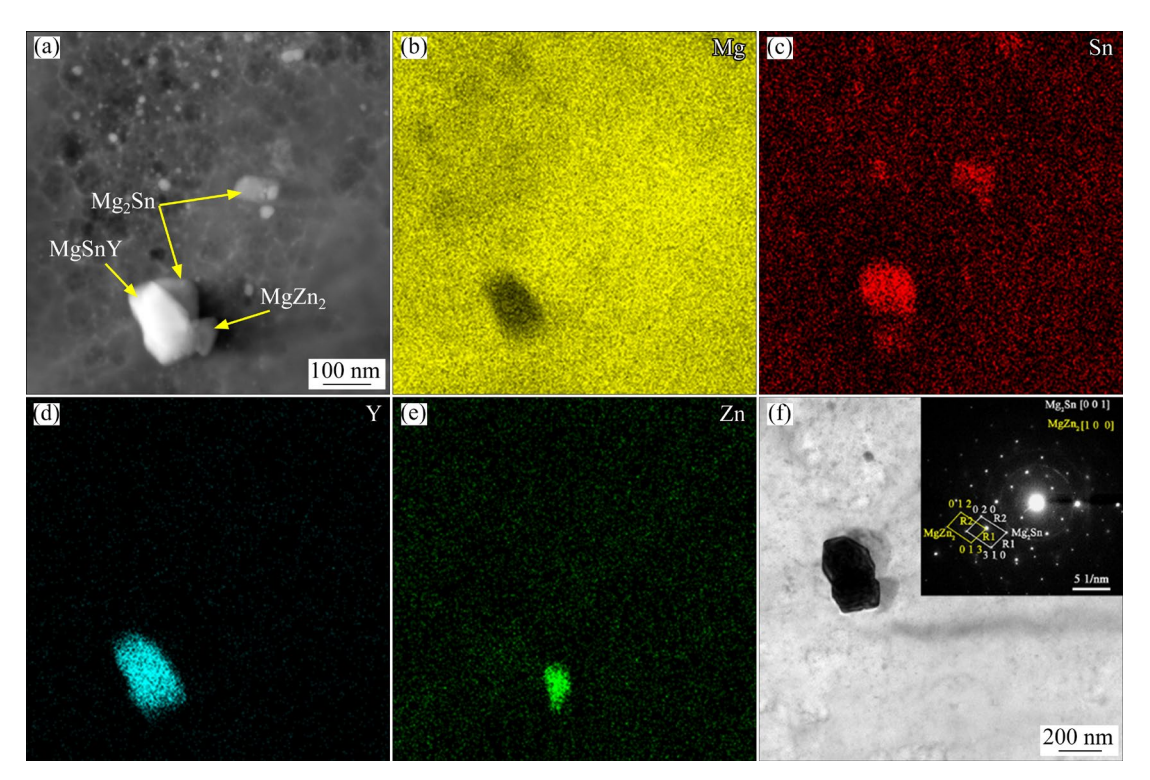


Fig. 3 TEM analysis results of T6-TZW711 alloy: (a) STEM image; (b-e) EDS elemental mappings of secondary phases; (f) TEM bright field image and SAED pattern of secondary phases

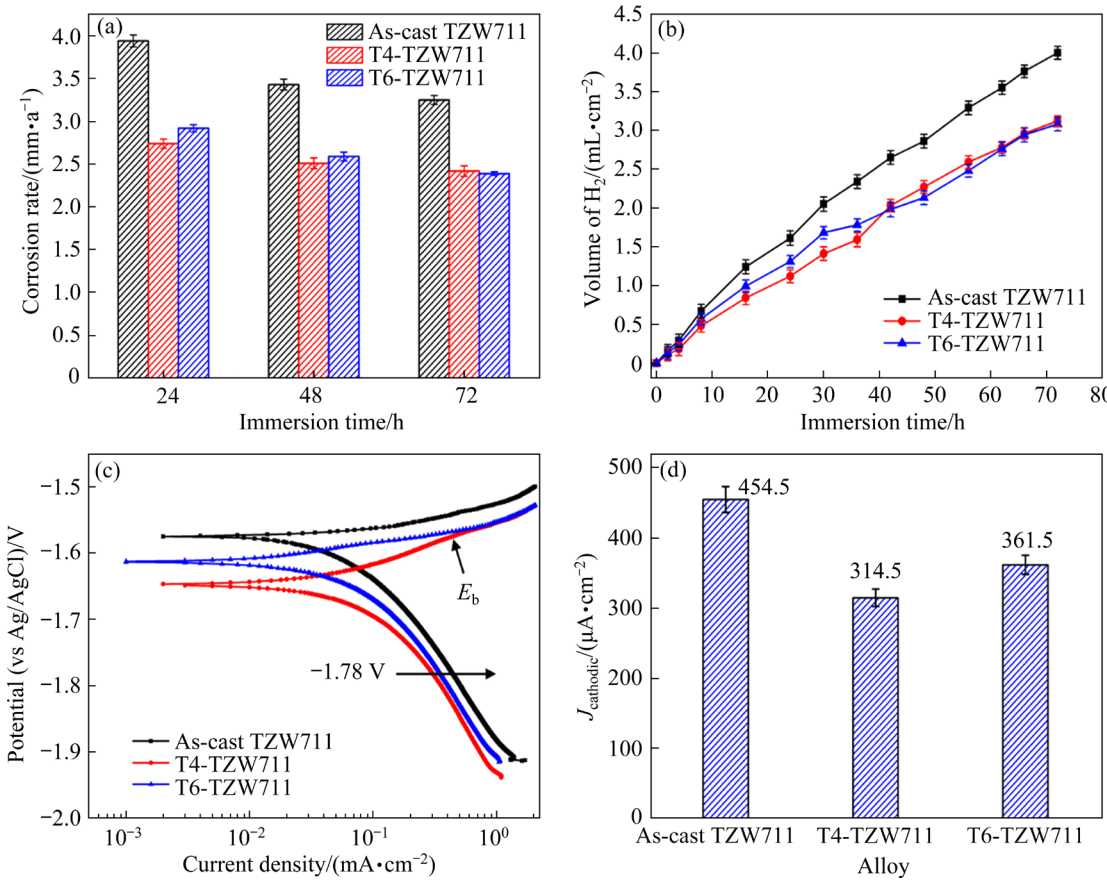


Fig. 4 Corrosion rates of Mg-7Sn-1Zn-1Y alloys after immersion in 3.5 wt.% NaCl solution for different time (a), hydrogen volume variation as function of immersion time (b), polarization curves (c), and cathodic current density measured at -1.78 V from polarization curves (d)

corrosion behavior of the T4-TZW711 alloy during the later corrosion stages. Figure 4(c) presents the potentiodynamic polarization curves of the Mg-7Sn-1Zn-1Y alloys. The anodic polarization curves of the as-cast TZW711 and T6-TZW711 alloys revealed that the alloys dissolved immediately after exceeding the corrosion potential. It can be clearly observed that the anodic polarization curve of the T4-TZW711 alloy had a small level of the breakdown potential (φ_b) , indicating that there was a passivation tendency between φ_b and the corrosion potential. Several previous studies [10,19,23,27] have suggested that the cathodic reaction can effectively describe the corrosion rate of Mg alloys due to the poor protectiveness of the corrosion film and the negative difference effect of the anode. Therefore, the cathodic current densities (J_{cathodic}) in the strong polarization region of the cathodic branch (-1.78 V) are demonstrated in Fig. 4(d) in order to reflect the corrosion rate of the alloys. The level of J_{cathodic} decreased from 454.5 µA/cm² for the as-cast

TZW711 alloy to $314.5 \,\mu\text{A/cm}^2$ for the T4-TZW711 alloy, indicating that the cathodic reaction of the former was significantly weakened after solution treatment.

In addition, EIS measurements were conducted to further elucidate the electrochemical behavior of the Mg-7Sn-1Zn-1Y alloys. The corresponding Nyquist and Bode plots are presented in Figs. 5(a) and (b), respectively. The Nyquist plots of all alloys exhibited a similar shape, with a capacitance loop between the high frequency (HF) and the medium frequency (MF), and an inductance loop at the low frequency (LF). The capacitance loop radius of the as-cast TZW711 alloy increased clearly after solution treatment. Moreover, the phase angle and |Z| (Z is the impedance of the alloy) values of the T4-TZW711 alloy were higher than those of the as-cast TZW711 alloy. This indicated that the corrosion resistance of the T4-TZW711 alloy was better than that of the as-cast TZW711 alloy. Figure 5(c) displays the equivalent circuit of the EIS curves and element characteristics of the

equivalent circuit, where R_s denotes the solution resistance, CPE_{dl} and R_{ct} denote the double-layer capacitance and charge transfer resistance, respectively, and L and R_L denote the inductance and the inductance resistance, respectively. In general, a CPE_{dl} in parallel with the R_{ct} is used to analyze the dissolution rate of Mg⁺ and Mg²⁺ at the interface between alloy and electrolyte [28], while L and R_L are used to analyze the adsorption of Mg⁺ and the occurrence of localized corrosion [29]. The fitting results are summarized in Table 2. It is noteworthy that CPE_{dl} is a non-ideal capacitor and can be defined as follows [30]:

$$CPE_{dl} = [Q(j\omega)^n]^{-1}$$
 (2)

where Q is the magnitude, j is the imaginary number, ω is the angular frequency, and n is the exponent. The T4-TZW711 alloy exhibited the lowest Q value.

Nonetheless, the fitted Q parameter cannot entirely represent the accurate value of the capacitance

 $(C_{\rm dl})$ [31]. The $C_{\rm dl}$ can reflect the corrosion area of the alloy surface; thus, it can be calculated by [32]

$$C_{\rm dl} = Q^{1/n} \left(\frac{R_{\rm s} R_{\rm ct}}{R_{\rm s} + R_{\rm ct}} \right)^{(1-n)/n}$$
 (3)

According to Fig. 6(a), the $C_{\rm dl}$ of the T4-TZW711 alloy was the lowest among all alloys, indicating that the corrosion area of its surface was minimal at the early stage of corrosion. As EIS data contain $R_{\rm ct}$ and $R_{\rm L}$, the polarization resistance $(R_{\rm p})$ is calculated to perform the direct comparison with the corrosion resistance. The $R_{\rm p}$ can be calculated through the following equation [33]:

$$R_{\rm p} = \frac{R_{\rm ct} R_{\rm L}}{R_{\rm ct} + R_{\rm L}} \tag{4}$$

Meanwhile, the value of $1/R_p$ (reciprocal of the polarization resistance), which is proportional to the corrosion rate, is given in Fig. 6(b). Both the T4-TZW711 and T6-TZW711 alloys exhibited lower $1/R_p$ values than the as-cast TZW711 alloy.

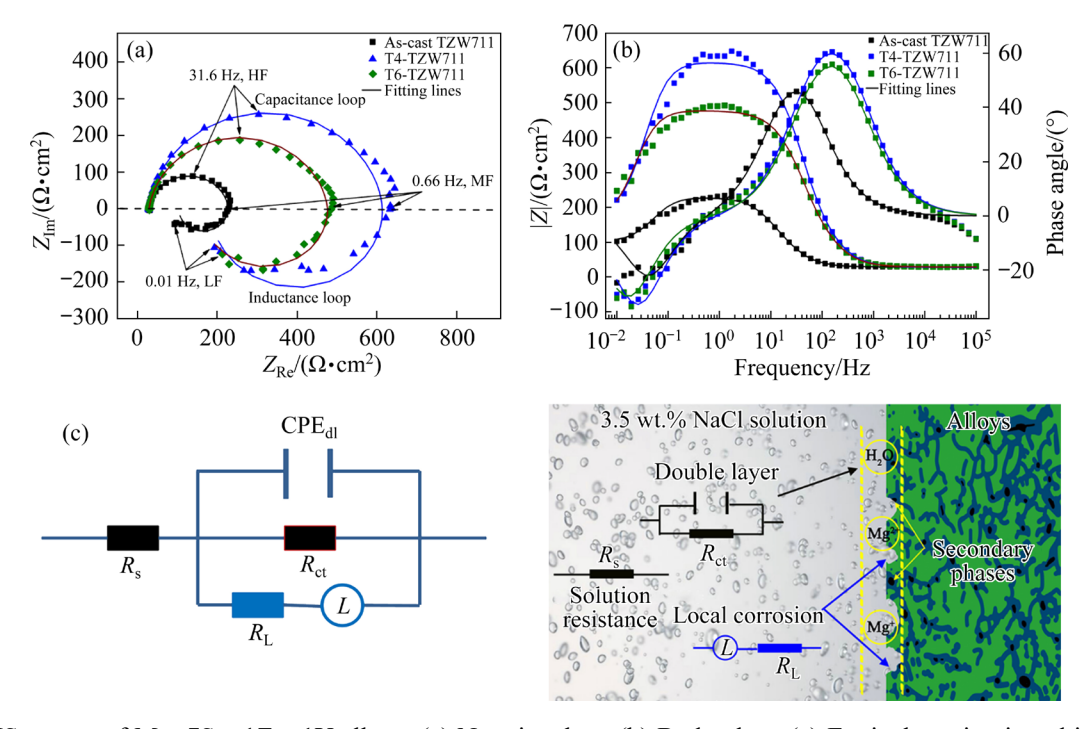


Fig. 5 EIS curves of Mg-7Sn-1Zn-1Y alloys: (a) Nyquist plots; (b) Bode plots; (c) Equivalent circuit and its element characteristics on alloy surface

Table 2 Equivalent circuit parameters used to fit EIS curves

Alloy	$R_{\rm s}/(\Omega\cdot{\rm cm}^2)$	$Q_{\mathrm{ct}}/(\mu\mathrm{F}\cdot\mathrm{cm}^{-2}\cdot\mathrm{s}^{n-1})$	$n_{\rm ct}$	$R_{\rm ct}/(\Omega\cdot{\rm cm}^2)$	$L/(\mathrm{H}\cdot\mathrm{cm}^{-2})$	$R_{\rm L}/(\Omega\cdot{\rm cm}^2)$
As-cast TZW711	29.4	99.93	0.939	196	865	94
T4-TZW711	28.5	13.65	0.927	588	2730	212
T6-TZW711	29.2	18.25	0.907	449	3536	187

3.3 Corrosion morphology

To better demonstrate the corrosion initiation process of Mg-7Sn-1Zn-1Y alloys obtained under different heat treatments, the corrosion morphologies of the alloys after immersion in 3.5 wt.% NaCl solution for 2 min are exhibited in Fig. 7. As it can be observed in Fig. 7(a), there were several apparent corrosion pits on the surface of the as-cast TZW711 alloy. The EDS analysis revealed that the corrosion products of the corrosion pits contained Mg, O, and Sn elements, but no Y element. This result indicated that the corrosion initiation sites generally occurred in regions enriched with Sn element, suggesting that the corrosion pits occurred around the Mg₂Sn phases. Nevertheless, the α-Mg around the bright MgSnY phases was slightly

corroded at the early stage of corrosion. Compared to the as-cast TZW711 alloy, the T4-TZW711 alloy exhibited a relatively uniform corrosion morphology, and only the α -Mg around the large MgSnY phase was corroded (Fig. 7(b)). After aging treatment, the corrosion pits on the T6-TZW711 alloy surface increased again, which can be attributed to the increase and scattered distribution of the secondary phases.

Figure 8 shows the corrosion morphologies of the Mg-7Sn-1Zn-1Y alloys after immersion in 3.5 wt.% NaCl solution for 72 h. As it can be observed in Figs. 8(a-c), the surfaces of all alloys were severely corroded. The surfaces of the as-cast TZW711 and T4-TZW711 alloys were completely covered by corrosion products, while the corrosion

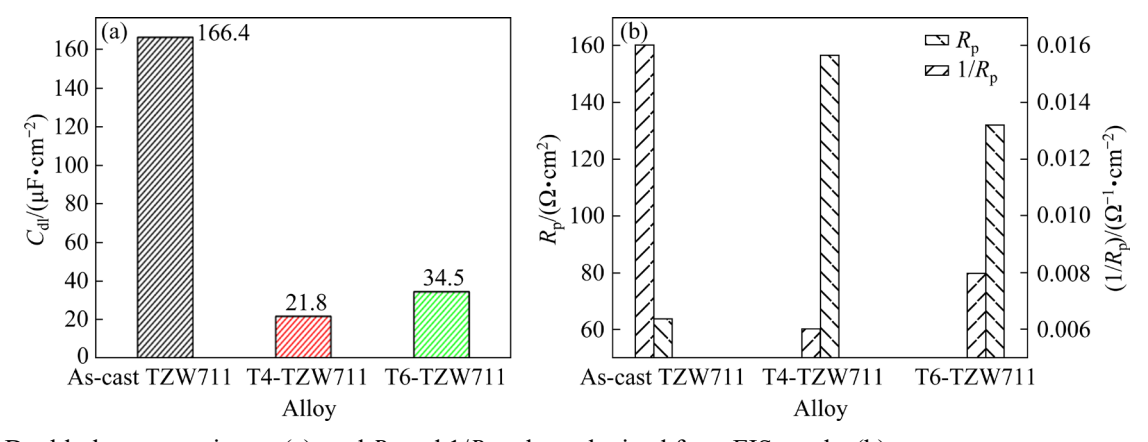


Fig. 6 Double-layer capacitance (a), and R_p and $1/R_p$ values obtained from EIS results (b)

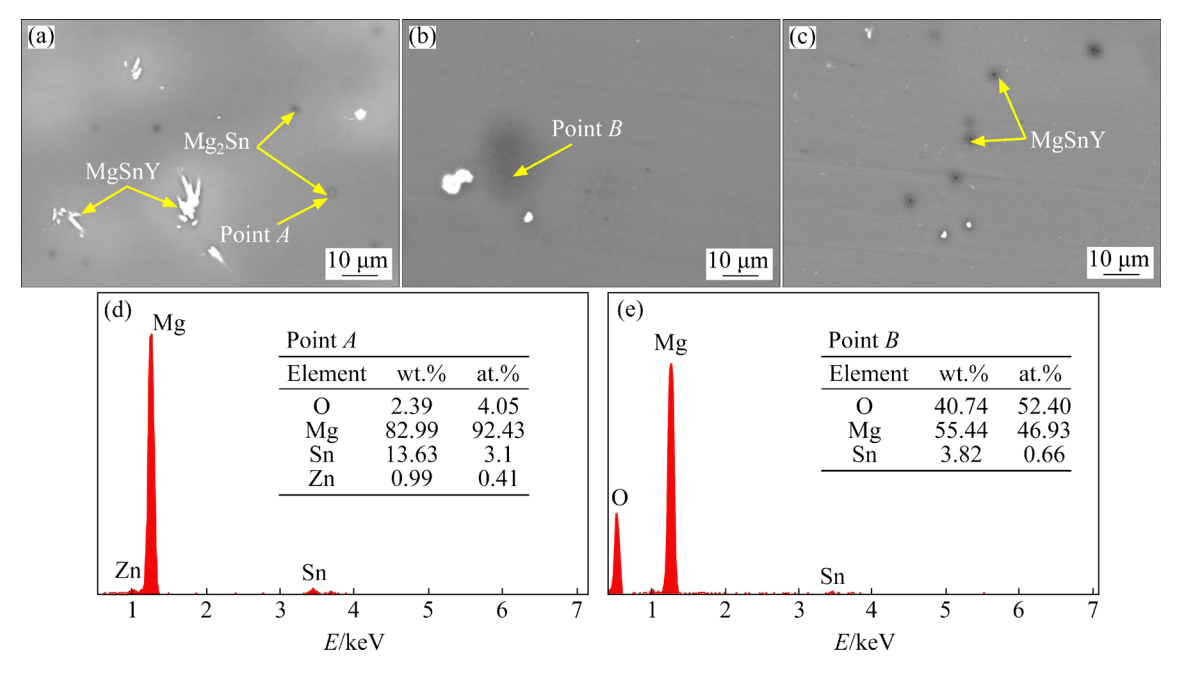


Fig. 7 Surface morphologies of Mg-7Sn-1Zn-1Y alloys after immersion in 3.5 wt.% NaCl solution for 2 min: (a) Ascast TZW711; (b) T4-TZW711; (c) T6-TZW711; (d, e) EDS results at Points A and B, respectively

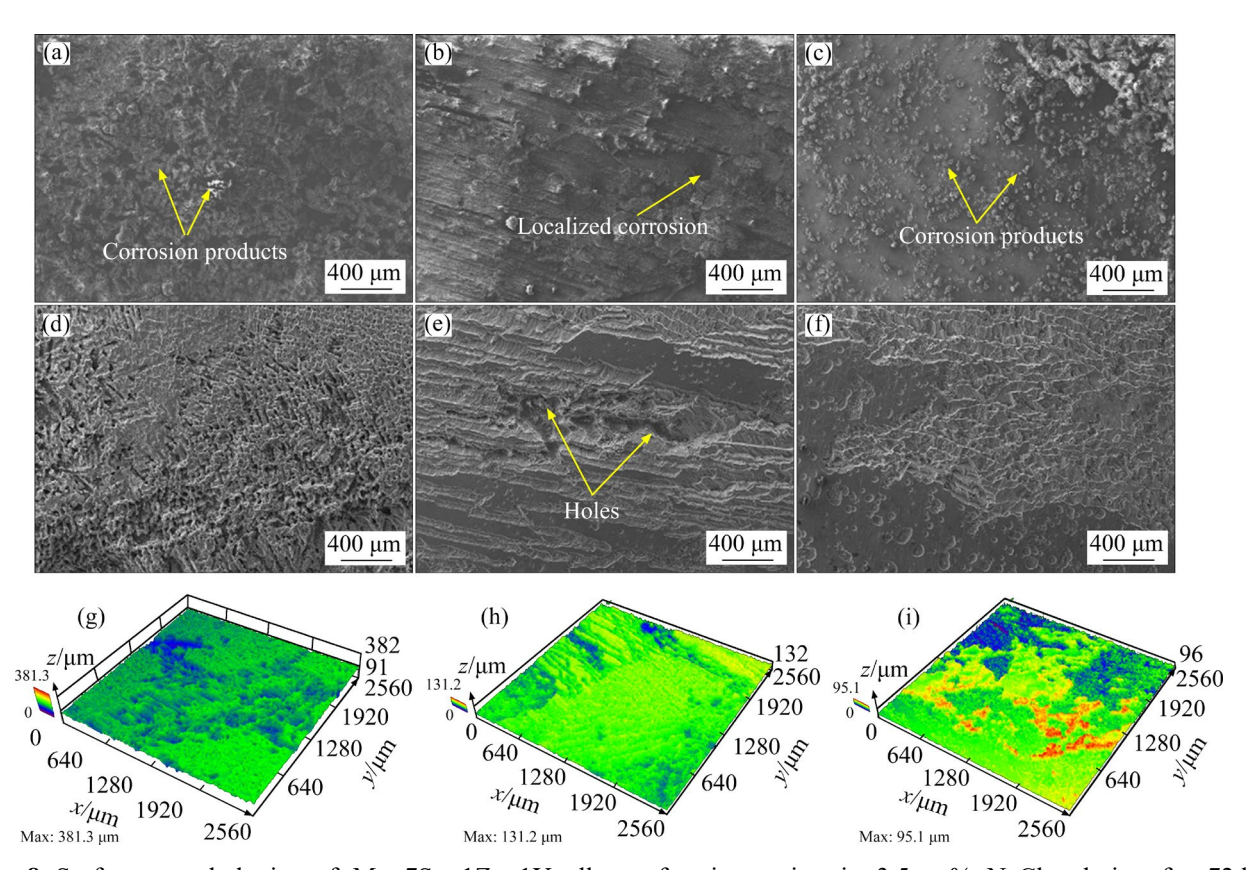


Fig. 8 Surface morphologies of Mg-7Sn-1Zn-1Y alloys after immersion in 3.5 wt.% NaCl solution for 72 h: (a-c) With corrosion products; (d-f) Without corrosion products; (g-i) 3D corrosion depth; (a, d, g) As-cast TZW711; (b, e, h) T4-TZW711; (c, f, i) T6-TZW711

products were significantly reduced, and some spherical corrosion products were formed on the T6-TZW711 alloy surface. As a result, the T6-TZW711 alloy achieved the greatest corrosion resistance after immersion for 72 h. Subsequently, the corrosion products were cleaned, and the surface morphology without corrosion products was captured, as presented in Figs. 8(d-f). The results indicated that localized corrosion occurred on the surface of all alloys. A large number of holes were observed on the as-cast TZW711 alloy surface, which grew laterally along the dendrite boundary. However, several shallow pits of localized corrosion were found on the T6-TZW711 alloy surface. To quantitatively characterize the localized corrosion depth, Figs. 8(g-i) show the 3D corrosion depth of the alloy surface after removing the corrosion products. The maximum corrosion depths of the as-cast TZW711, T4-TZW711, and T6-TZW711 alloys were measured to be 381.3, 131.2, and 95.1 µm, respectively. Therefore, the T6-TZW711 alloy possessed the lowest sensitivity of localized corrosion after immersion for 72 h.

4 Discussion

During the corrosion process of the Mg-7Sn-1Zn-1Y alloys in 3.5 wt.% NaCl solution, the dissolution of metal ions at the anode and reduction reaction of water molecules at the cathode occur simultaneously to induce the generation of corrosion products on the alloy surfaces. Figure 9 presents the XPS analysis results for the T6-TZW711 alloy after immersion in 3.5 wt.% NaCl solution for 72 h. The spectra suggest that the Mg 1s peak comprised two components. The binding energies at 1303.8 and 1305.3 eV match to MgO and Mg(OH)₂, respectively [34]. The Sn 3d spectrum exhibited two peaks due to the spin orbit splitting into Sn $3d_{3/2}$ and Sn $3d_{5/2}$ components, i.e., one at 486.4 eV and the other at 494.9 eV. These values are in agreement with the value of SnO₂ [35]. In the Zn 2p spectrum, a weak peak of ZnO was observed, suggesting that a small amount of ZnO corrosion product was formed on the alloy surface. Unfortunately, no peaks of Y-containing corrosion

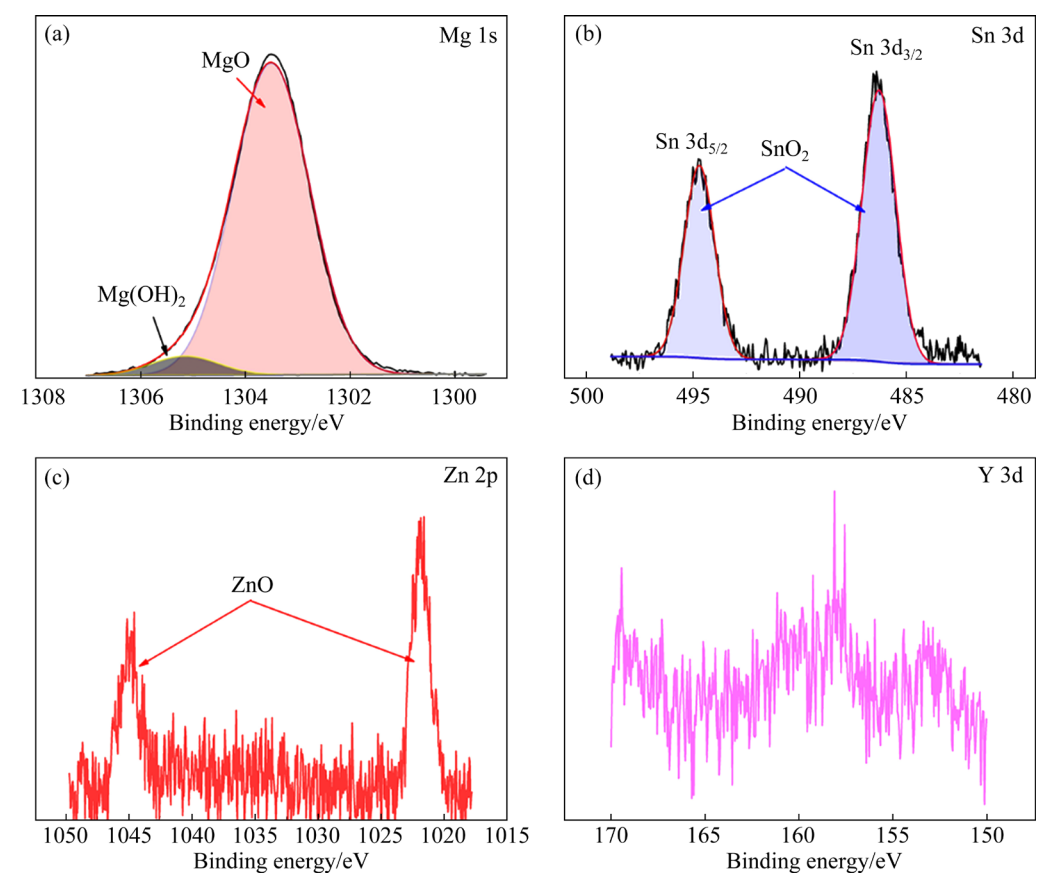


Fig. 9 XPS analysis results of T6-TZW711 alloy after immersion in 3.5 wt.% NaCl solution for 72 h

products were found in the Y 3d spectrum because the fraction of these products was too small to be detected on the alloy surface.

The corrosion products of Mg(OH)₂ are easily adsorbed by Cl⁻ ions through the following reactions [36]:

$$Mg(OH)_2+Cl^-=MgOHCl_{ad}+OH^-$$
 (5)

$$MgOHCl_{ad}=Mg^{2+}+OH^{-}+Cl^{-}$$
 (6)

Moreover, the content of ZnO and Y₂O₃ corrosion products with good thermodynamic stability on the alloy surface was too low. These resulted in the poor protection of the corrosion film. After immersion for only 2 min, pitting corrosion occurred on the alloy surface (Fig. 7). Therefore, the effect of the corrosion products on corrosion resistance is minor and the corrosion behavior of the Mg-7Sn-1Zn-1Y alloys depends mainly on the type, size, morphology, and distribution of the secondary phases.

The as-cast TZW711 alloy was composed of α -Mg matrix, Mg₂Sn, MgSnY, and Sn element enriched areas. At the early stage of corrosion, local

micro-galvanic corrosion occurred between the α -Mg matrix and the secondary phases. HA et al [10] reported that the Mg₂Sn phases act mainly as the cathode of micro-galvanic corrosion in Mg-Sn alloys, which is due to the high difference in the corrosion potential between Mg₂Sn and α-Mg matrix. Figure 7 also indicates that micro-galvanic corrosion begins preferentially around the Mg₂Sn phases. In general, the standard electrode potential of the Y element is much lower than that of Sn [37]. Y-containing secondary phases have been reported to exhibit a low corrosion potential [38,39]. Evidently, the MgSnY phase which incorporates the lower potential of the Y element can exhibit a lower corrosion potential than the Mg₂Sn phase. The effect of the MgSnY phase as the cathode of micro-galvanic corrosion is weaker than that of the Mg₂Sn phase. Consequently, the corrosion around the MgSnY phases of the as-cast TZW711 alloy after immersion for 2 min was mild. Compared to the as-cast TZW711 alloy, the T4-TZW711 alloy contained only MgSnY phase (Fig. 2). LÜ et al [40] reported that the MgSnY phase has a high melting point and is difficult to dissolve into the α -Mg matrix even at 500 °C. The eliminated Mg₂Sn phase and element enrichment areas can reduce the cathodic current density (Fig. 4(c)), which increased the dissolution resistance (R_{ct}) and reduced the corrosion rate of the T4-TZW711 alloy (Fig. 4(a)). Unfortunately, the clustered MgSnY led to the high inductive reactance still existing in the EIS curve of the T4-TZW711 alloy. After aging treatment, the area fraction of the undissolved MgSnY phase in the T6-TZW711 alloy increased and its distribution became more dispersed. YU et al [41] also found that the clustered secondary phases of Mg-Y-Sn alloys are dispersed during isothermal oxidation. The dispersed MgSnY phases increased the amount of local micro-galvanic corrosion sites, thereby increasing the corrosion rate of the T6-TZW711 alloy at the early corrosion stage. Thus, after immersion for 24 h, the corrosion rate of the T6-TZW711 alloy was higher than that of the T4-TZW711 alloy (Fig. 4(a)).

After immersion in 3.5 wt.% NaCl solution for 72 h, severe localized corrosion and the maximum corrosion depth were observed on the surface of the as-cast TZW711 alloy. Most of α -Mg around dendrites fell off because the Mg₂Sn and MgSnY act as the cathode to increase the localized corrosion rate. According to the mixed potential theory [42]:

$$\ln J_{\text{corr}}^{\text{Mix}} = \frac{\beta_{\text{c}}^{\text{SP}}}{\beta_{\text{a}}^{\text{Mg}} + \beta_{\text{c}}^{\text{SP}}} \ln \left(A_{\text{SP}} \cdot J_{\text{corr}}^{\text{SP}} \right) +$$

$$\frac{\beta_{\text{a}}^{\text{Mg}}}{\beta_{\text{a}}^{\text{Mg}} + \beta_{\text{c}}^{\text{SP}}} \ln \left(A_{\text{Mg}} \cdot J_{\text{corr}}^{\text{Mg}} \right) + \frac{\varphi_{\text{corr}}^{\text{SP}} - \varphi_{\text{corr}}^{\text{Mg}}}{\beta_{\text{a}}^{\text{Mg}} + \beta_{\text{c}}^{\text{SP}}}$$
(7)

where A_{SP} (SP: secondary phase) is the contact area between the secondary phases and the electrolyte, $\beta_{\rm a}^{\rm Mg}$ and $\beta_{\rm c}^{\rm SP}$ are the Tafel slopes of α -Mg and the secondary phases, respectively, and $\varphi_{\rm corr}^{\rm Mg}$ and $\varphi_{\rm corr}^{\rm SP}$ are the corrosion potentials of α -Mg and the secondary phases, respectively. It can be deduced that the occurrence of corrosion depends on the Tafel slope and corrosion potential of the secondary phases, while the corrosion degree depends on the areas of the secondary phases. The as-cast TZW711 alloy possessed the largest secondary phase area and exhibited the highest corrosion rate. However, it is worth noting that, after immersion for 72 h, the corrosion rate of the T6-TZW711 alloy was slightly lower than that of the T4-TZW711 alloy. This result does not agree with the corrosion rate after immersion for 24 h and the electrochemical measurement results, which may be due to the alteration of the corrosion behavior of the T4-TZW711 and T6-TZW711 alloys with increasing immersion time. Figure 10 presents the cross-sectional corrosion morphologies of the Mg-7Sn-1Zn-1Y alloys after immersion in 3.5 wt.% NaCl solution for 72 h by the EPMA analysis. It can be observed that the clustered MgSnY phase peeled off from the T4-TZW711 alloy surface. This can lead to the formation of corrosion holes (Fig. 8(e)). The detachment of the nonuniform MgSnY phase with α -Mg matrix may have rapidly increased the instantaneous corrosion rate of the T4-TZW711 alloy. This speculation is demonstrated by the rapid increase in the hydrogen evolution rate of the T4-TZW711 alloy during the later corrosion stages. As it can be observed in Figs. 10(d-i), the inner layer of corrosion products was enriched with Sn and a few Y elements, indicating that the effect of the precipitated Mg₂Sn and MgSnY phases on the corrosion process was weaker than that of the undissolved MgSnY phases. WU et al [43] reported that the nano-sized secondary phases do not significantly deteriorate the corrosion process of Mg alloys. The relationship between the galvanic corrosion current density and the secondary phase size can be given as [43,44]

$$J_{\rm F} \approx \varphi_{\rm corr}^{\rm c} - \varphi_{\rm corr}^{\rm a} / \left(\frac{L^{\rm a}}{L^{\rm c}} \rho_{\rm p}^{\rm c} + \rho_{\rm p}^{\rm a} \right)$$
 (8)

where $J_{\rm F}$ is the galvanic corrosion current density, $L^{\rm a}$ and $L^{\rm c}$ are the lengths of the anode and cathode, respectively, and $\rho_{\rm p}^{\rm a}$ and $\rho_{\rm p}^{\rm c}$ are the polarization resistivity of the anode and cathode respectively. The value of $L^{\rm c}$ for the precipitated Mg₂Sn and MgSnY phases is negligible, suggesting that the contribution of the precipitated Mg₂Sn and MgSnY phases on galvanic corrosion current density is insignificant. Consequently, the corrosion rate of the T6-TZW711 alloy depends mainly on the undissolved MgSnY phases.

5 Conclusions

(1) The corrosion products of Mg-7Sn-1Zn-1Y alloys were mainly composed of Mg(OH)₂, MgO, SnO₂, and a small amount of ZnO, while no Y-containing corrosion product was detected on alloy surface. Most of the Y element existed in the form of MgSnY secondary phase, which resulted in

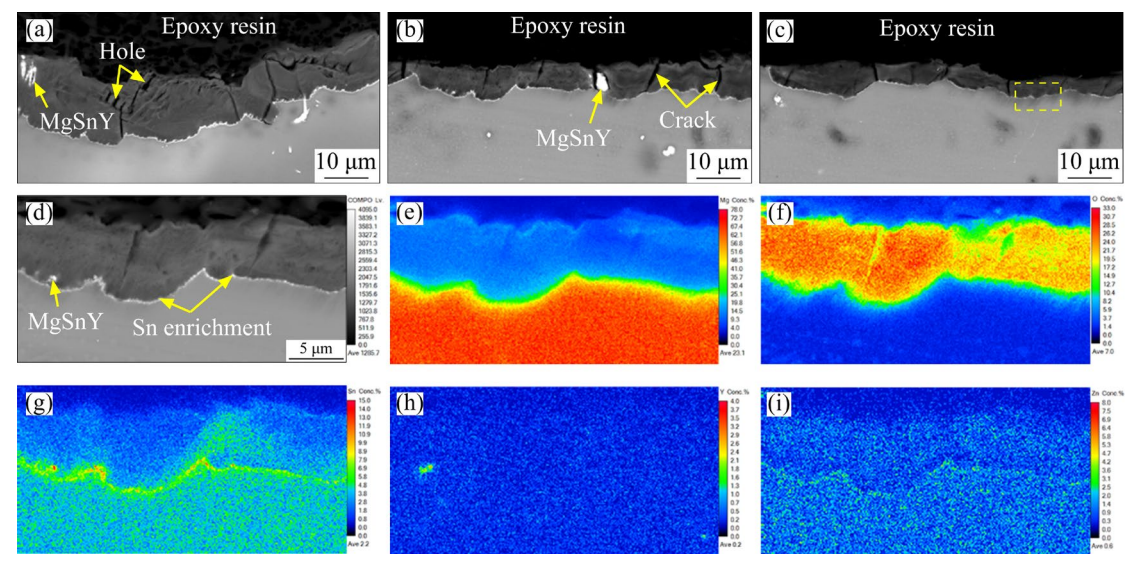


Fig. 10 Cross-sectional corrosion morphologies of Mg-7Sn-1Zn-1Y alloys after immersion in 3.5 wt.% NaCl solution for 72 h by EPMA analysis: (a) As-cast TZW711; (b) T4-TZW711; (c) T6-TZW711; (d) Magnification image of rectangular area in (c); (e-i) Mg, O, Sn, Y, and Zn elements, respectively

the poor protection of the corrosion film. The as-cast TZW711, T4-TZW711, and T6-TZW711 alloys all underwent severe localized corrosion.

- (2) In the early corrosion stage, the T4-TZW711 alloy exhibited the lowest corrosion rate because the effect of the MgSnY phase as the cathode of micro-galvanic corrosion was weaker than that of the Mg2Sn phase. The dissolution of Mg2Sn reduced the cathodic current density, increased the charge transfer resistance, and thus decreased the corrosion rate of the T4-TZW711 alloy.
- (3) After immersion in 3.5 wt.% NaCl solution for 72 h, the clustered MgSnY phases were detached from the T4-TZW711 alloy surface. Consequently, the corrision rate and localized corrosion depth of the T4-TZW711 alloy were slightly higher than those of the T6-TZW711 alloy. Moreover, the corrosion rate of the T6-TZW711 alloy depended mainly on the undissolved MgSnY phases rather than the nano-sized precipitated Mg2Sn and MgSnY phases.

CRediT authorship contribution statement

Xue-jian WANG: Conceptualization, Methodology, Data curation, Writing — Original draft, Software; Hua-qiang XIAO: Resources, Data curation, Writing — Review & editing, Funding acquisition; Chong WANG: Methodology, Investigation, Visualization; En-yu GUO: Validation, Formal analysis, Writing — Review & editing, Supervision, Funding acquisition; Tong-min WANG:

Conceptualization, Supervision, Project administration; **Bo LIN:** Investigation, Methodology, Resources.

Declaration of competing interest

The authors declare that they have no known competing financial interests or personal relationships that could have appeared to influence the work reported in this paper.

Acknowledgments

This work was supported by the National Natural Science Foundation of China (Nos. 52301041, 52022017, 52065009, 52371005), the Special Fund for Special Posts of Guizhou University, China (No. [2023]26), the Science and Technology Planning Project of Guizhou Province, China (No. ZK2021269), and the Fundamental Research Funds for the Central Universities, China (No. DUT23YG104).

References

- [1] AMIR B, HAMID K, SEYED MAHDI M. Microstructural evolution and creep properties of Mg-4Sn alloys by addition of calcium up to 4 wt.% [J]. Transactions of Nonferrous Metals Society of China, 2020, 30: 896–904.
- [2] ZHONG Li-ping, WANG Yong-jian, DOU Yu-chen. On the improved tensile strength and ductility of Mg-Sn-Zn-Mn alloy processed by aging prior to extrusion [J]. Journal of Magnesium and Alloys, 2019, 7(4): 637-647.
- [3] GENG Hao-ran, WANG Qing-lei, LIU Peng, WU Ming. Effects of P addition on the microstructure and mechanical properties of Mg-5%Sn-1.25%Si alloy [J]. International Journal of Minerals, Metallurgy, and Materials, 2014, 21(3):

- 289-294.
- [4] ZHAO Chao-yue, CHEN Xian-hua, PAN Fu-sheng, GAO Shang-yu, ZHAO Di, LIU Xiao-fang. Effect of Sn content on strain hardening behavior of as-extruded Mg-Sn alloys [J]. Materials Science and Engineering: A, 2018, 713: 244–252.
- [5] CHENG Wei-li, QUE Zhong-ping, ZHANG Jin-shan, XU Chun-xiang, LIANG Wei, YOU B S, PARK S S. Compressive deformation behavior of an indirect-extruded Mg-8Sn-1Al-1Zn alloy [J]. International Journal of Minerals, Metallurgy, and Materials, 2013, 20(1): 49-56.
- [6] WEI Shang-hai, CHEN Yun-gui, TANG Yong-bai, LIU Hong-mei, XIAO Su-fen, NIU Gao, ZHANG Xiao-ping, ZHAO Yuan-hua. Compressive creep behavior of as-cast and aging-treated Mg-5wt.%Sn alloys [J]. Materials Science and Engineering: A, 2008, 492(1): 20–23.
- [7] SASAKI T T, ELSAYED F R, NAKATA T, OHKUBO T, KAMADO S, HONO K. Strong and ductile heat-treatable Mg-Sn-Zn-Al wrought alloys [J]. Acta Materialia, 2015, 99: 176-186.
- [8] HA HY, KANG JY, KIM SG, KIM B, PARK SS, YIM CD, YOU B S. Influences of metallurgical factors on the corrosion behaviour of extruded binary Mg-Sn alloys [J]. Corrosion Science, 2014, 82: 369-379.
- [9] KIM H J, KIM B, BAEK S M, SOHN S D, SHIN H J, JEONG H Y, YIM C D, YOU B S, HA H Y, PARK S S. Influence of alloyed Al on the microstructure and corrosion properties of extruded Mg-8Sn-1Zn alloys [J]. Corrosion Science, 2015, 95: 133-142.
- [10] HA H Y, KIM H J, BAEK S M, KIM B, SOHN S D, SHIN H J, JEONG H Y, PARK S H, YIM C D, YOU B S, LEE J G, PARK S S. Improved corrosion resistance of extruded Mg-8Sn-1Zn-1Al alloy by microalloying with Mn [J]. Scripta Materialia, 2015, 109: 38-43.
- [11] MAHDI S, HASSAN J, RAMAN S. Effect of extrusion parameters on degradation of magnesium alloys for bioimplant applications: A review [J]. Transactions of Nonferrous Metals Society of China, 2022, 32(9): 2787–2813.
- [12] ABU LEIL T, HORT N, DIETZEL W, BLAWERT C, HUANG Y, KAINER K U, RAO K P. Microstructure and corrosion behavior of Mg-Sn-Ca alloys after extrusion [J]. Transactions of Nonferrous Metals Society of China, 2009, 19(1): 40-44.
- [13] RADHA R, SREEKANTH D. Mechanical and corrosion behaviour of hydroxyapatite reinforced Mg-Sn alloy composite by squeeze casting for biomedical applications [J]. Journal of Magnesium and Alloys, 2020, 8(2): 452–460.
- [14] LIU Xian-bin, SHAN Da-yong, SONG Ying-wei, CHEN Rong-shi, HAN En-hou. Influences of the quantity of Mg₂Sn phase on the corrosion behavior of Mg-7Sn magnesium alloy [J]. Electrochimica Acta, 2011, 56(5): 2582–2590.
- [15] WANG Xue-jian, CHEN Zong-ning, ZHANG Yu-bo, GUO En-yu, KANG Hui-jun, HAN Pei, WANG Tong-min. Influence of microstructural characteristics on corrosion behavior of Mg-5Sn-3In alloy in Hank's solution [J]. Transactions of Nonferrous Metals Society of China, 2021, 31(10): 2999-3011.
- [16] LIU Qiang, CHENG Wei-li, ZHANG Hui, XU Chun-xiang, ZHANG Jin-shan. The role of Ca on the microstructure and

- corrosion behavior of Mg-8Sn-1Al-1Zn-Ca alloys [J]. Journal of Alloys and Compounds, 2014, 590: 162-167.
- [17] WANG Xue-jian, CHEN Zong-ning, GUO En-yu, LIU Xue-qin, KANG Hui-jun, WANG Tong-min. The role of Ga in the microstructure, corrosion behavior and mechanical properties of as-extruded Mg-5Sn-xGa alloys [J]. Journal of Alloys and Compounds, 2021, 863: 158762.
- [18] HUANG Xue-fei, HAN Guo-min, HUANG Wei-gang. T6 treatment and its effects on corrosion properties of an Mg-4Sn-4Zn-2Al alloy [J]. Materials, 2018, 11(4): E628.
- [19] HA H Y, KANG Jun-yun, YIM C D, YANG Jie, YOU B S. Role of hydrogen evolution rate in determining the corrosion rate of extruded Mg-5Sn-(1-4 wt.%)Zn alloys [J]. Corrosion Science, 2014, 89: 275-285.
- [20] YANG Hua-bao, WU Liang, JIANG Bin, LIU Wen-jun, XIE Hong-mei, SONG Jiang-feng, HUANG Guang-sheng, ZHANG Ding-fei, PAN Fu-sheng. Effect of microstructure on the corrosion behavior of as-cast and extruded Mg-Sn-Y alloys [J]. Journal of the Electrochemical Society, 2020, 167(12): 121503.
- [21] LIU Jin-hui, SONG Ying-wei, CHEN Jia-chen, CHEN Peng, SHAN Da-yong, HAN En-hou. The special role of anodic second phases in the micro-galvanic corrosion of EW75 Mg alloy [J]. Electrochimica Acta, 2016, 189: 190–195.
- [22] JAFARI H, TEHRANI A H M, HEYDARI M. Effect of extrusion process on microstructure and mechanical and corrosion properties of biodegradable Mg-5Zn-1.5Y magnesium alloy [J]. International Journal of Minerals, Metallurgy and Materials, 2022, 29(3): 490-502.
- [23] WANG Xue-jian, CHEN Zong-ning, REN Jing, KANG Hui-jun, GUO En-yu, LI Jie-hua, WANG Tong-min. Corrosion behavior of as-cast Mg-5Sn based alloys with In additions in 3.5 wt.% NaCl solution [J]. Corrosion Science, 2020, 164: 108318.
- [24] WANG Pan-pan, JIANG Hai-tao, WANG Yu-jiao, ZHANG Yun, TIAN Shi-wei, ZHANG Ye-fei, CAO Zhi-ming. Role of trace additions of Ca and Sn in improving the corrosion resistance of Mg-3Al-1Zn alloy [J]. International Journal of Minerals, Metallurgy and Materials, 2022, 29(8): 1559–1569.
- [25] ZHAO C Y, PAN F S, ZHAO S, PAN H C, SONG K, TANG A T. Microstructure, corrosion behavior and cytotoxicity of biodegradable Mg-Sn implant alloys prepared by sub-rapid solidification [J]. Materials Science and Engineering: C, 2015, 54: 245-251.
- [26] WANG Peng-qi, GUO En-yu, WANG Xue-jian, KANG Hui-jun, CHEN Zong-ning, CAO Zhi-qiang, WANG Tong-min. The influence of Sc addition on microstructure and tensile mechanical properties of Mg-4.5Sn-5Zn alloys [J]. Journal of Magnesium and Alloys, 2019, 7(3): 456-465.
- [27] BAEK S M, KANG J S, KIM J C, KIM B, SHIN H J, PARK S S. Improved corrosion resistance of Mg-8Sn-1Zn-1Al alloy subjected to low-temperature indirect extrusion [J]. Corrosion Science, 2018, 141: 203-210.
- [28] BARIL G, GALICIA G, DESLOUIS C, PÉBÈRE N, TRIBOLLET B, VIVIER V. An impedance investigation of the mechanism of pure magnesium corrosion in sodium sulfate solutions [J]. Journal of the Electrochemical Society, 2007, 154(2): C108-C113.

- [29] CAO Fu-yong, SONG Guang-ling, ATRENS A. Corrosion and passivation of magnesium alloys [J]. Corrosion Science, 2016, 111: 835–845.
- [30] JORCIN J B, ORAZEM M E, PÉBÈRE N, TRIBOLLET B. CPE analysis by local electrochemical impedance spectroscopy [J]. Electrochimica Acta, 2006, 51(8): 1473–1479.
- [31] ORAZEM M E, FRATEUR I, TRIBOLLET B, VIVIER V, MARCELIN S, PÉBÈRE N, BUNGE A L, WHITE E A, RIEMER D P, MUSIANI M. Dielectric properties of materials showing constant-phase-element (CPE) impedance response [J]. Journal of the Electrochemical Society, 2013, 160(6): C215-C225.
- [32] HIRSCHORN B, ORAZEM M E, TRIBOLLET B, VIVIER V, FRATEUR I, MUSIANI M. Determination of effective capacitance and film thickness from constant-phase-element parameters [J]. Electrochimica Acta, 2010, 55(21): 6218–6227.
- [33] ZHANG T, SHAO Y W, MENG G Z, CUI Z Y, WANG F H. Corrosion of hot extrusion AZ91 magnesium alloy: I—Relation between the microstructure and corrosion behavior [J]. Corrosion Science, 2011, 53(5): 1960–1968.
- [34] SONG Ying-wei, HAN En-hou, DONG Kai-hui, SHAN Da-yong, YIM C D, YOU B S. Microstructure and protection characteristics of the naturally formed oxide films on Mg-xZn alloys [J]. Corrosion Science, 2013, 72: 133–143.
- [35] YIN Ming, HOU Li-feng, LIU Xiao-da, WANG Zhi-wei, LIU Bao-sheng, JIA Jian-wen, ZHANG Shao-hua, WEI Ying-hui. Tailoring the micromorphology of the as-cast Mg-Sn-In alloys to corrosion-resistant microstructures via adjusting In concentration [J]. Journal of Alloys and Compounds, 2019, 811: 152024.
- [36] KUBÁSEK J, VOJTĚCH D, LIPOV J, RUML T. Structure, mechanical properties, corrosion behavior and cytotoxicity of biodegradable Mg–X (X=Sn, Ga, In) alloys [J]. Materials

- Science and Engineering: C, 2013, 33(4): 2421-2432.
- [37] BRATSCH G G. Standard electrode potentials and temperature coefficients in water at 298.15 K [J]. Journal of Physical and Chemical Reference Data, 1989, 18: 1–21.
- [38] BAEK S M, LEE S Y, KIM J C, KWON J, JUNG H, LEE S, LEE K S, PARK S S. Role of trace additions of Mn and Y in improving the corrosion resistance of Mg-3Al-1Zn alloy [J]. Corrosion Science, 2021, 178: 108998.
- [39] JIA Rui-ling, ZHANG Ming, ZHANG Li-na, ZHANG Wei, GUO Feng. Correlative change of corrosion behavior with the microstructure of AZ91 Mg alloy modified with Y additions [J]. Journal of Alloys and Compounds, 2015, 634: 263–271.
- [40] LÜ Dong-xian, GUO Cui-ping, LI Chang-rong, DU Zhenmin. Thermodynamic description of Sn-Y and Mg-Sn-Y systems [J]. Journal of Rare Earths, 2014, 32(7): 648-654.
- [41] YU Xiao-wen, JIANG Bin, YANG Hong, YANG Qing-shan, XIA Xiang-sheng, PAN Fu-sheng. High temperature oxidation behavior of Mg-Y-Sn, Mg-Y, Mg-Sn alloys and its effect on corrosion property [J]. Applied Surface Science, 2015, 353: 1013–1022.
- [42] WANG Xue-jian, CHEN Zhong-ning, GUO En-yu, KANG Hui-jun, CAO Zhi-qiang, FU Ya-nan, WANG Tong-min. Corrosion process of Mg-Sn alloys revealed via in situ synchrotron X-ray radiography [J]. Materials Letters, 2022, 308: 131139.
- [43] WU Peng-peng, SONG Guang-ling, ZHU Yi-xing, FENG Zhen-liang, ZHENG Da-jiang. The corrosion of Al-supersaturated Mg matrix and the galvanic effect of secondary phase nanoparticles [J]. Corrosion Science, 2021, 184: 109410.
- [44] SONG Guang-ling. Potential and current distributions of one-dimensional galvanic corrosion systems [J]. Corrosion Science, 2010, 52(2): 455–480.

第二相对 Mg-7Sn-1Zn-1Y 合金腐蚀行为的影响

王雪健1, 肖华强1, 王 冲2, 郭恩宇2,3, 王同敏2,3, 林 波1

- 1. 贵州大学 机械工程学院, 贵阳 550000;
- 2. 大连理工大学 材料科学与工程学院 凝固控制与数字化制备技术辽宁省重点实验室, 大连 116024;
 - 3. 大连理工大学 宁波研究院, 宁波 315000

摘 要:通过显微组织表征、质量损失实验、析氢实验、电化学测试和腐蚀形貌观察等手段研究了第二相对经固溶(T4)和时效(T6)热处理后铸态 Mg-7Sn-1Zn-1Y(TZW711)合金腐蚀行为的影响。结果表明: T4-TZW711 合金在早期腐蚀阶段具有最高的耐蚀性,这是因为 Mg2Sn 的固溶降低了合金的阴极电流密度,并增加了合金的电荷转移电阻(Ret)。但当腐蚀时间延长时,未固溶且聚集的 MgSnY 相从 T4-TZW711 合金表面剥落,从而提高其腐蚀速率。经时效热处理后,未固溶的 MgSnY 相分布变得离散,使 T6-TZW711 合金的局部腐蚀敏感性低于 T4-TZW711 合金。此结果表明,T6 处理能提高 Mg-7Sn-1Zn-1Y 合金的耐蚀性。

关键词: Mg-Sn-Zn-Y 合金; 热处理; MgSnY 相; 电化学测试; 腐蚀行为